PROCEEDINGS OF SCIENCE

Search for Dark Matter in association with an energetic photon in pp collisions at $\sqrt{s} = 13$ TeV with the ATLAS detector

F. Piazza, on behalf of the ATLAS Collaboration[a,*]

[a] *Dipartimento di Fisica, Università di Milano and INFN, Sezione di Milano, Via Celoria 16, Milano, Italy*

E-mail: federica.piazza@mi.infn.it

A search for Dark Matter (DM) is presented, exploiting final states containing a photon and missing transverse momentum, using 139 fb^{-1} of data collected by the ATLAS experiment (LHC) at a centre-of-mass energy of 13 TeV. The discriminant variable is the missing transverse momentum ($E_{\mathrm{T}}^{\mathrm{miss}}$): several signal regions are defined in bins of $E_{\mathrm{T}}^{\mathrm{miss}}$ to enhance the analysis sensitivity, and associated control regions (CRs) are built to derive background expectations by normalizing Monte Carlo (MC) yields to data through a likelihood fit simultaneously performed over all the CRs. This strategy allows combining inputs from all the CRs coherently, taking into account the correlations of systematic uncertainties among different regions. No deviations are observed relative to the predictions of the Standard Model and 95% confidence level (CL) upper limits between 2.4 fb and 0.5 fb are set on the visible cross section of physics beyond the Standard Model, in different ranges of $E_{\mathrm{T}}^{\mathrm{miss}}$. The results are interpreted as exclusion limits in simplified DM models, where weakly interacting DM candidates are pair-produced via an s-channel axial-vector or vector mediator. The search excludes mediator masses below 920-1470 GeV for DM candidate masses below 280-580 GeV at 95% CL, depending on the couplings. These results are translated into exclusion limits on the interaction cross-section between DM and nucleons as a function of the DM mass, and compared with the limits currently set by direct detection experiments, underlying a good complementarity between the two detection strategies. In addition, the results are expressed in terms of 95% CL limits on the parameters of a model with an axion-like particle produced in association with a photon.

Corfu Summer Institute 2021 "School and Workshops on Elementary Particle Physics and Gravity"
29 August - 9 October 2021
Corfu, Greece

*Speaker

PoS(CORFU2021)098

1. Introduction

According to astrophysical and cosmological observations, Dark Matter (DM) accounts for about 27% of the universe's mass. Despite compelling evidences of its existence as an invisible and gravitationally interacting component of matter, non-gravitational interactions with ordinary matter have never been confirmed so far, and its nature and properties are still largely unknown, resulting in a plethora of possible DM models and candidates, in a wide range of masses [1].
The search at colliders provides a complementary approach to DM detection with respect to direct detection and indirect detection experiments. In particular, if an interaction between DM and ordinary matter exists, DM particles can, in principle, be produced in high energy proton-proton collisions happening at the Large Hadron Collider (LHC) at CERN. Being DM candidates stable and weakly interacting with Standard Model (SM) particles, a DM particle produced at LHC would not decay nor be directly detected by the experiments. If produced in association with a SM particle, though, they can lead to the so-called X+$E_{\mathrm{T}}^{\mathrm{miss}}$ signature, characterized by an unbalance in the total transverse momentum of the final state, known as missing transverse momentum ($E_{\mathrm{T}}^{\mathrm{miss}}$), recoiling against a visible SM particle, X (a photon γ, a jet, a W/Z boson or a Higgs boson) [2].
This report focuses on an analysis in the γ+$E_{\mathrm{T}}^{\mathrm{miss}}$ final state (mono-photon), performed using the full Run 2 dataset, collected between 2015 and 2018 by the ATLAS experiment at a centre-of-mass energy of 13 TeV and corresponding to a total integrated luminosity of 139 fb^{-1}[3]. The increased statistics, together with optimization of selection criteria and physical objects reconstruction, ensures an enhanced sensitivity of the analysis with respect to previous publication based on a dataset of 36.2 fb^{-1} [4]. These results are part of an extensive program of DM searches at LHC, carried out within the ATLAS collaboration. In particular the X+$E_{\mathrm{T}}^{\mathrm{miss}}$ searches focus on simplified DM models of WIMPs production (Weakly Interacting Massive Particles): with respect to the other X+$E_{\mathrm{T}}^{\mathrm{miss}}$ searches, the γ+$E_{\mathrm{T}}^{\mathrm{miss}}$ final state is second in sensitivity only to the jet+$E_{\mathrm{T}}^{\mathrm{miss}}$ one [5] and takes advantage of a cleaner final state. In addition, the results of the mono-photon analysis are interpreted also in terms of ALPs (Axion-Like Particles).

2. The ATLAS detector

The ATLAS experiment [6] at the LHC is a multipurpose particle detector with a forward–backward symmetric cylindrical geometry and a near 4π coverage in solid angle.[1] It consists of an inner tracking detector surrounded by a thin superconducting solenoid providing a 2 T axial magnetic field, electromagnetic and hadron calorimeters, and a muon spectrometer. The inner tracking detector covers the pseudorapidity range $|\eta| < 2.5$. It consists of silicon pixel, silicon microstrip, and transition radiation tracking detectors. Lead/liquid-argon (LAr) sampling calorimeters provide electromagnetic (EM) energy measurements with high granularity. A steel/scintillator-tile hadron calorimeter covers the central pseudorapidity range ($|\eta| < 1.7$). The endcap and forward regions

[1] ATLAS uses a right-handed coordinate system with its origin at the nominal interaction point (IP) in the centre of the detector and the z-axis along the beam pipe. The x-axis points from the IP to the centre of the LHC ring, and the y-axis points upwards. Cylindrical coordinates (r, ϕ) are used in the transverse plane, ϕ being the azimuthal angle around the z-axis. The pseudorapidity is defined in terms of the polar angle θ as $\eta = -\ln\tan(\theta/2)$. Angular distance is measured in units of $\Delta R \equiv \sqrt{(\Delta\eta)^2 + (\Delta\phi)^2}$.

are instrumented with LAr calorimeters for both the EM and hadronic energy measurements up to $|\eta| = 4.9$. The muon spectrometer surrounds the calorimeters and is based on three large superconducting air-core toroidal magnets with eight coils each. The field integral of the toroids ranges between 2 and 6 T/m across most of the detector. The muon spectrometer includes a system of precision tracking chambers and fast detectors for triggering. A two-level trigger system is used to select events. The first-level trigger is implemented in hardware and uses a subset of the detector information to accept events at a rate below 100 kHz. This is followed by a software-based trigger that reduces the accepted event rate to 1 kHz on average depending on the data-taking conditions.

3. Signal models

Beyond Standard Model (BSM) processes with a γ+$E_{\mathrm{T}}^{\mathrm{miss}}$ signature are predicted in several models. Among these, this analysis focuses on Simplified DM models of WIMPs production and on an Effective Field Theory (EFT) of ALPs production [7].

Simplified DM models proposed by the ATLAS/CMS DM Forum [8][9] consist of a minimum extension of the SM, predicting an additional Dirac-fermion WIMP candidate, produced through s-channel with vector or axial-vector mediator, in association with a photon from Initial State Radiation (fig. 1a). The main advantage of simplified DM models is their ability to describe the full DM kinematics better than an EFT, without adding the full complexity of a complete theory, thus depending on a small number of free parameters: the DM (m_χ) and mediator (m_{med}) masses, the couplings of the mediator to the quarks (g_q), leptons (g_l) and DM (g_χ) particles, and the mediator width Γ_{med}, which is fixed to the minimal value allowed by the given choice of the couplings and of the mediator and DM masses.

ALPs, firstly introduced as a possible solution to the strong CP problem of the SM [10], can be either non-thermal DM candidates or mediators to a dark-sector [11]. An EFT [7] is explored in this report (fig. 1b), based on an extension of the SM lagrangian with an additional CP-odd singlet under the SM charges, arising as a (pseudo-)Nambu-Goldstone boson of a spontaneously broken symmetry at a scale f_a higher than the electroweak scale. The free parameters are the f_a scale, together with the $c_{\tilde{W}}$, one of the real operator coefficients c_i in the effective Lagrangian describing bosonic ALP couplings. The $c_{\tilde{B}}$ coefficient is fixed to $c_{\tilde{B}} = -\tan^2(\theta)c_{\tilde{W}}$, based on the assumption of null coupling to two photons, motivated by strong experimental constraints.

4. Data and MC simulations

The analysis has been performed on the full Run 2 dataset, selecting only good quality data, acquired with stable beams conditions and in good operational status of all ATLAS detector components.

The Sherpa Monte Carlo (MC) generator has been used to generate MC samples at NLO for the SM background processes, together with Geant4 [12] for the full simulation of the particles interaction with the ATLAS detector [13]. The signal MC samples have been produced at NLO with the MadGraph5_aMC@NLO generator [14], in association with Pythia8 [15] for the parton shower simulation, hadronization and underlying events modelling. Both background and signal MC samples include the simulation of inelastic collisions in the same or neighbouring bunch crossing

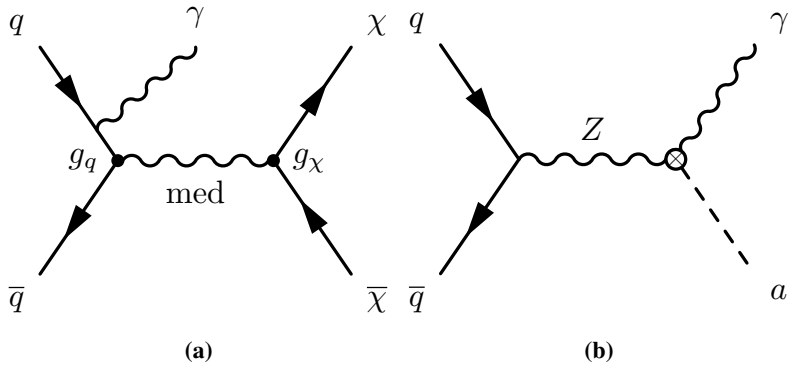

Figure 1: Feynman diagrams of the simplified DM model for WIMP production (a) and EFT model for ALPs production (b).

(pile-up) and are reweighted in order to reproduce the pile-up conditions observed in data.
For the simplified DM models, since the analysis acceptance is independent on the spin structure, couplings, and m_χ for fixed m_{med} in the on-shell region, only the axial-vector scenario with g_q= 0.25 and g_χ= 1 has been produced at reconstruction level, for masses in the transition region from on-shell to off-shell regime, and for m_χ=10 GeV and varying m_{med}. These MC samples were processed through a fast simulation of the ATLAS detector using a parameterisation of the calorimeter response and Geant4 for the inner detector and muon spectrometer. The other considered signals, with vector mediator or different couplings and different explored masses, have been produced at truth-level only, to derive their cross section: for these scenarios, the results can be obtained by means of a cross section rescaling of the ones produced at reconstruction-level.
For ALPs production model, one sample, with $c_{\tilde{W}} = 1$, $m_{ALP} = 1$ MeV, $f_a = 1$ TeV, has been produced with fast simulation. Different masses and parameters values are explored by cross section rescaling, with a similar procedure as for simplified DM models.
Data and MC samples undergo the same event reconstruction, combining information from (real or simulated) signals in each sub-detector to describe the final state.

5. Analysis strategy

The key discriminant variable of the analysis is $E_{\mathrm{T}}^{\mathrm{miss}}$, defined as the module of the negative vectorial sum ($\mathbf{p}_{\mathrm{T}}^{\mathrm{miss}}$) of the transverse momenta of all the reconstructed particles (hard objects) and of the tracks matched to the primary vertex and not associated to any physics particle (soft-term) [16].
An appropriate event selection is applied to define the signal regions (SRs) of the analysis, while associated control regions (CRs) are built to derive background expectations by normalizing MC yields to data.

5.1 Event selection

The same event selection is applied to both data and MC simulations. A trigger pre-selection requires at least one photon with $p_{\mathrm{T}} > 140$ GeV. In addition, a primary vertex must be reconstructed

Table 1: Definition of the analysis Signal Regions (SRs) [3].

	SRI1	SRI2	SRI3	SRI4	SRE1	SRE2	SRE3
$E_{\mathrm{T}}^{\mathrm{miss}}$[GeV]	> 200	> 250	> 300	> 375	[200, 250]	[250, 300]	[300, 375]

with at least two associated good-quality tracks, and events containing a poor-quality photon or jet arising from instrumental problems or non-collision background are removed.
The SR is defined by requiring at least one photon with transverse momentum $p_{\mathrm{T}}>$ 150 GeV and $\Delta\phi(\mathbf{p}_{\mathrm{T}}^{\gamma}, \mathbf{p}_{\mathrm{T}}^{\mathrm{miss}}) > 0.4$, and vetoing electrons, muons or hadronically decaying taus, in order to reject events with a W or Z boson produced in association with a photon or jet. Up to one jet is accepted, to suppress multi-jet background, with an additional selection on $\Delta\phi(\mathbf{p}_{\mathrm{T}}^{\mathrm{jet}}, \mathbf{p}_{\mathrm{T}}^{\mathrm{miss}})$ applied to reject γ+jets events where the $E_{\mathrm{T}}^{\mathrm{miss}}$ arises from energy mismeasurements or misreconstruction of the photon or the jets. To further reduce the γ+ jets background, a selection cut has been optimized on the $E_{\mathrm{T}}^{\mathrm{miss}}$ significance variable [17], required to be higher than 8.5, since this variable provides a high discrimination power between $E_{\mathrm{T}}^{\mathrm{miss}}$ from undetected particles and that arising from detector effects.
In order to enhance the analysis sensitivity, four inclusive SRs with increasing $E_{\mathrm{T}}^{\mathrm{miss}}$ thresholds are defined. In addition, three exclusive SRs corresponding to different $E_{\mathrm{T}}^{\mathrm{miss}}$ bins, are introduced to allow a simplified shape-fit, as described in the following sub-section. The definition of all SRs is summarized in table 1. Thanks to the increased statistics, an optimization of the SRs thresholds and of the bins width have been possible, adding one more inclusive and one more exclusive SR with respect to the previously published analysis with 36.2 fb^{-1}[4].

5.2 The background estimation

The γ+$E_{\mathrm{T}}^{\mathrm{miss}}$ signature can be produced by several SM processes. Among these, the dominant and only irreducible background is constituted by $\gamma + Z(\rightarrow \nu\nu)$ events, but other processes can mimic the signal final state due to detector effects: $\gamma + Z(\rightarrow \ell\ell)$ and $\gamma + W(\rightarrow \ell\nu)$, can contribute to the background in case of inefficiencies in lepton reconstruction; γ+jet, if high $E_{\mathrm{T}}^{\mathrm{miss}}$ is produced by a miscalibration or misreconstruction of a jet or a photon, or in case of wrong jet-to-primary vertex association; jets or electrons can be misidentified as photons (jet/$e \rightarrow \gamma$ background), giving contribution to the background mainly in W/Z+jets events. The background estimation relies on the comparison between data and MC simulations for the dominant backgrounds with real photons, while data-driven techniques are employed to estimate the subleading jet/$e \rightarrow \gamma$ background.

5.2.1 Real-photon backgrounds

Contributions from the dominant γ+$Z(\rightarrow \nu\nu)$ background and from γ+$Z(\rightarrow \ell\ell)$, γ+$W(\rightarrow \ell\nu)$ and γ+jets are estimated using specific CRs, defined by inverting one or more cuts of the SR, in order to enhance the contribution of each background process, while suppressing the signal. The 1-muon CR (CR1mu) for the $\gamma + W(\rightarrow \ell\nu)$ background estimation is defined by requiring exactly one muon in the event. Two CRs, the 2-muons (CR2mu) and 2-electrons (CR2el) are defined for γ+$Z(\rightarrow \nu\nu)$ and γ+$Z(\rightarrow \ell\ell)$ background, requiring exactly two muons (electrons) and vetoing the other leptons. In order to reproduce the SR kinematics in these lepton-CR, the leptons are treated as invisible particles in the $E_{\mathrm{T}}^{\mathrm{miss}}$ calculation, by subtracting the corresponding terms. Finally, a low

$E_{\mathrm{T}}^{\mathrm{miss}}$ γ+jet CR (CRphjet) is defined with 85 GeV $< E_{\mathrm{T}}^{\mathrm{miss}} <$ 110 GeV, with an additional higher threshold $\Delta\phi(\mathbf{p}_{\mathrm{T}}^{\gamma}, \mathbf{p}_{\mathrm{T}}^{\mathrm{miss}}) < 3.0$ to reduce possible signal contamination. The $E_{\mathrm{T}}^{\mathrm{miss}}$ significance cut is removed in all CRs.

5.2.2 Backgrounds from electron/jets misidentified as photons

The jet $\rightarrow \gamma$ background [3] estimation in each analysis region is performed through a two side-band method (ABCD), based on the definition of three background-regions (B, C, D) enriched with events containing photons from misidentified jets. Photons in the analysis region (A) are required to satisfy identification criteria based on shower shape variables and be isolated from nearby signals in the calorimeter, while the B, C and D regions are obtained by reverting one or both these identification and isolation requirements.
The $e \rightarrow \gamma$ background [3] in each analysis region is estimated by scaling the event yield in the so-called probe-electron CRs (defined as the analysis region, but requiring an electron in place of the photon) by the probability (fake-rate) for such an electron to be reconstructed as a photon. The fake-rate is derived from a data sample of $Z \rightarrow ee$ events, where reconstructed photons are expected to come from misidentified electrons.

5.3 Background-only fit

A background-only maximum likelihood fit, simultaneously performed over all the CRs using the HistFitter package [18], is performed to normalize MC predictions to data. This fit combines inputs from all the CRs coherently, taking into account the correlations of the systematic uncertainties among different regions.
The MC predictions in each SR and CR, as well as the data-driven estimates, are given in input to the likelihood as fixed parameters. The background yields for real-photon backgrounds are allowed to float in the fit through their associated normalization factors, included as free parameters in the likelihood. Finally, systematic uncertainties are treated as nuisance parameter, with a gaussian constraint. The final background yield is derived by extrapolating to the SR the normalization factors obtained from the fit in the CRs. Two fit strategies are used: the "single-bin" fit is performed separately for each inclusive $E_{\mathrm{T}}^{\mathrm{miss}}$ bin, combining all the associated CRs; the "simplified shape-fit" is performed simultaneously over all the exclusive bins and last inclusive one, providing an instrument to exploit the $E_{\mathrm{T}}^{\mathrm{miss}}$ shape information, thus enhancing the analysis sensitivity thanks to an improved discrimination between signal and background.

6. Results

The background-only fit is performed to derive the expected SM yields in all the SRs and CRs. The systematic uncertainties include both experimental and theoretical contributions [3]. The first ones are related to energy and momentum scales and resolution of the physics objects, their identification, reconstruction and isolation efficiencies, the soft-term scale and resolution and the uncertainty on the integrated luminosity measurement and pile-up reweighting. Systematic uncertainties arising from the jet/$e \rightarrow \gamma$ background estimates are also taken into account. The theoretical uncertainties from MC simulations are related to QCD factorisation and renormalisation scales, the value of the strong coupling constants and the choice of parton distribution functions

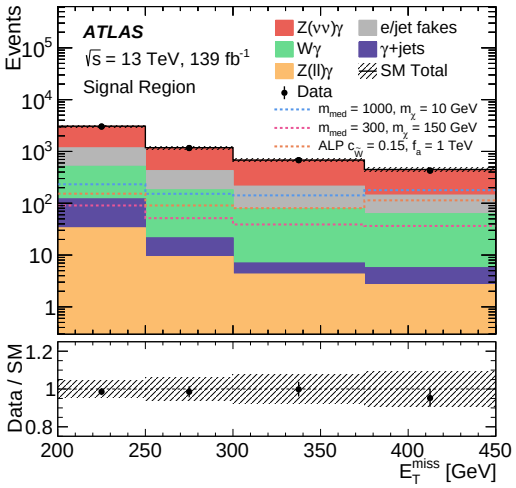

Figure 2: $E_{\mathrm{T}}^{\mathrm{miss}}$ distribution for data and SM expectations after the simplified-shape fit. The low panel shows the ratio between data and background. The error bars represent data statistical uncertainty, while the dashed band the systematic and statistical background uncertainties. Three signal samples are also shown as dashed lines [3].

Table 2: Statistical and systematic uncertainties in each SR of the analysis [3].

	SRI1	SRI2	SRI3	SRI4	SRE1	SRE2	SRE3
Stat+Syst [%]	3.5	4.8	6.2	952	4.3	6.3	7.8
Stat [%]	2.4	3.6	5.3	8.5	3.3	5.0	6.7

(PDFs).

After the background-only fit, the background in the first inclusive SR is composed by 63% of $\gamma+Z(\rightarrow \nu\nu)$, by 21% of jets/electrons misidentifies as photons, by 13% of $\gamma+W(\rightarrow \ell\nu)$ and by 2% of γ+jets and by less than 1% of $\gamma+Z(\rightarrow \ell\ell)$. A comparison of $E_{\mathrm{T}}^{\mathrm{miss}}$ distribution between data and background expectations after the simplified-shape fit is shown in fig. 2. The distributions for three signals, as an example, are shown as well, in dashed lines. In the low panel, the ratio between data and background estimation in each bin is reported. Finally, figs. 3a and 3b summarize the results of the single-bin and simplified-shape fit respectively in all SRs and CRs. Post-fit background expectations are compared to data. As shown in the bottom panels, reporting the significance of the discrepancies between data and background expectations, there is a good agreement in all regions, and no significant excess with respect to SM expectations in the SRs is observed.

The systematic and statistical uncertainties obtained from the fit are summarized in table 2, showing that the analysis is generally dominated by statistical uncertainties. From a comparison of the relative impact of each source of systematic uncertainty on the background yields, it emerges that the dominant ones come from jets (ranging from 1.4% to 4.1%) and electrons (2%-2.3%) misidentified as photons, together with jet energy scale and resolution (1.6% - 2.7%). The other experimental systematics have relative impact below 1.5%, while theoretical uncertainties do not exceed 0.5%.

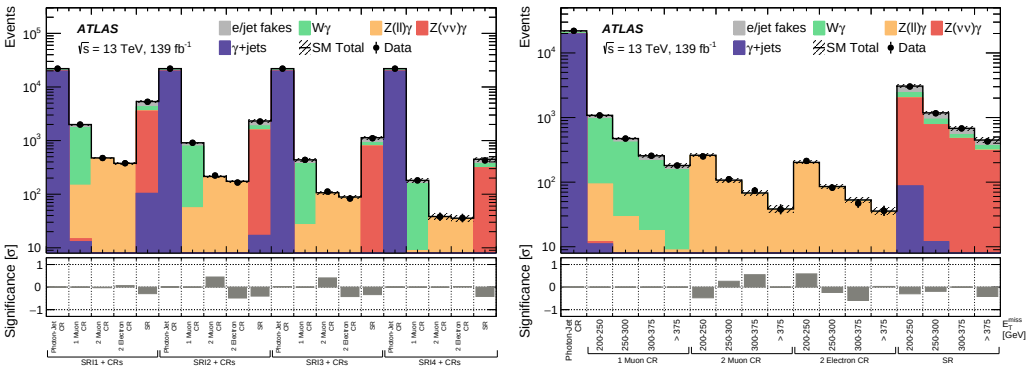

(a) **(b)**

Figure 3: Data event yields and SM predictions from the background-only single-bin (a) and simplified-shape fit (b). Statistical and systematic uncertainties are shown. In the lower panel, the significance of the difference between data and background is shown [3].

7. Interpretation of the results

Results are interpreted in terms of exclusion upper limits on the simplified DM and ALPs production models, as well as model-independent limits on the visible cross section of BSM processes. The likelihood fits are based on the profile-likelihood-ratio test statistics [18] and CLs prescriptions [19].

7.1 Model-dependent limits

A simplified shape-fit is performed on fast simulated signal samples, in both SRs and associated CRs, including the signal yields as a fixed parameter and the signal strength as freely floating normalization factor: a specific signal is excluded if the upper limit at 95% CL on its signal strength is lower than 1. Results for different parameters are obtained by cross section rescaling, as mentioned in sect. 4.

The exclusion limits for the simplified DM models are reported in the m_{med}-m_{χ} plane in fig. 4, for scenarios with axial-vector or vector mediator and different couplings to quarks and leptons. Systematic uncertainties on the signal acceptance and cross section [3] are included, accounting for QCD factorization and renormalization scale and choice of PDFs (less than 5%), together with uncertainties in initial- and final-state radiation due to the choice of parton shower parameters (less than 10%). Only the acceptance uncertainties are included in the fit, while cross section ones are indicated as dotted lines around the observed limit. The band represents the $\pm 1\sigma$ variations including all background and signal acceptance uncertainties. The area below the contours are excluded. Depending on the couplings, the maximum excluded values are: 920-1460 GeV for m_{med} and 280-415 GeV for m_{χ} in the axial-vector scenario, 950-1470 GeV for m_{med} and 400-580 GeV for m_{χ} in the vector scenario.

In order to show the complementarity with DM direct detection searches, the contours in the m_{χ}-m_{med} plane, obtained for a specific choice of mediator and couplings, can be directly translated

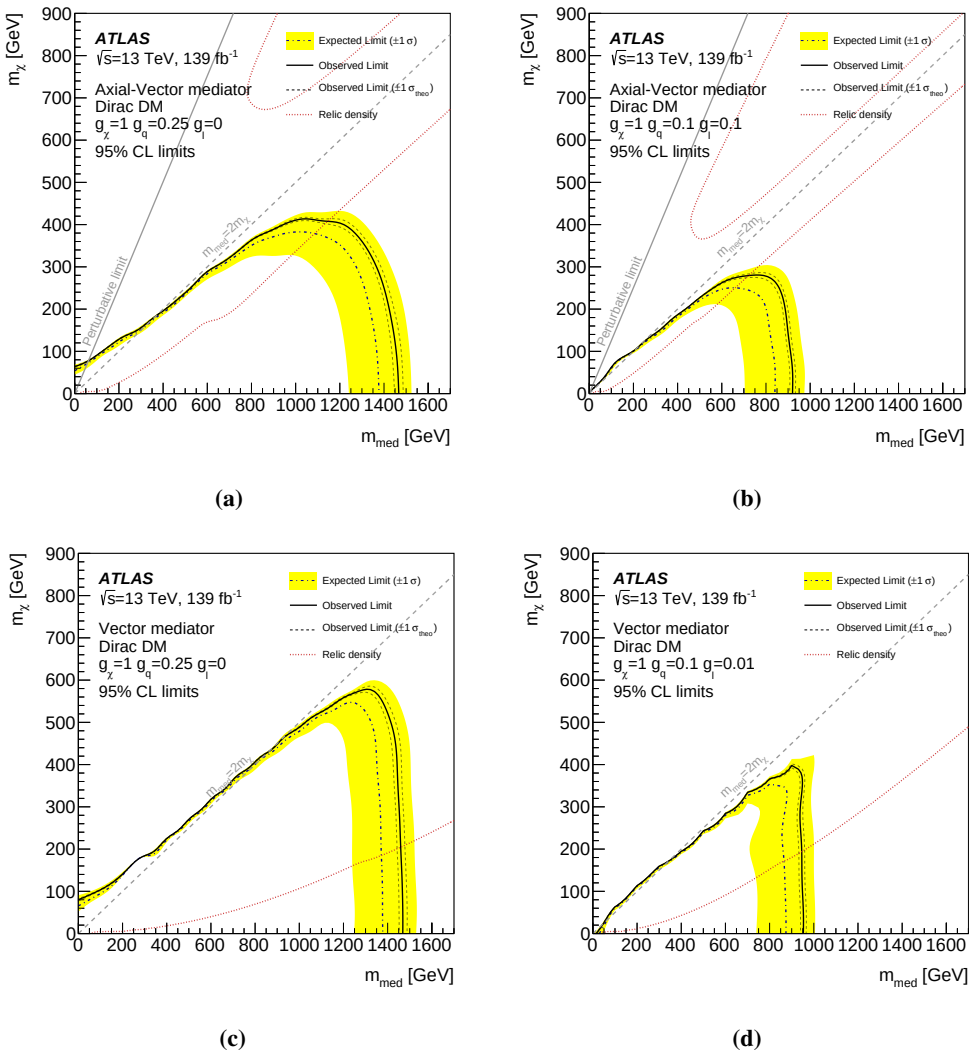

Figure 4: The observed (solid line) and expected (dot-dashed line) 95% CL exclusion contours in the m_χ–m_{med} plane for a simplified DM model with: axial-vector mediator and couplings $g_\chi = 1$, $g_q = 0.25$ and $g_\ell = 0$ (top-left) and $g_\chi = 1$, $g_q = 0.1$ and $g_\ell = 0.1$ (top-right); vector mediator and couplings $g_\chi = 1$, $g_q = 0.25$ and $g_\ell = 0$ (bottom-left) and $g_\chi = 1$, $g_q = 0.1$ and $g_\ell = 0.01$ (bottom-right). The area under the limit curve is excluded. The region to the left of the $m_\chi = \sqrt{\pi/2}m_{\text{med}}$ line is excluded by the perturbative limit for axial-vector mediators [20]. The area below the relic density [21] curve in the on-shell region (or above in the off-shell region in the axial-vector mediator case) corresponds to a predicted DM overabundance [3].

into bounds on the χ–nucleon scattering cross section following the procedure described in Ref. [22] Figure 5a and 5b show the 90% CL exclusion limits on the χ–proton and χ–neutron spin-dependent (SD) scattering cross section versus m_χ in the axial-vector model with couplings g_q= 0.25, g_χ= 1 and g_l= 0. The mono-photon analysis probes complementary regions with respect to direct DM searches ([23–28]) in the full parameters space, providing greater sensitivity for m_χ values below 380 GeV. Finally, Figure 5c shows the 90 %CL exclusion limits on the χ-nucleon spin-independent (SI) scattering cross section versus m_χ for the vector model with couplings g_q=

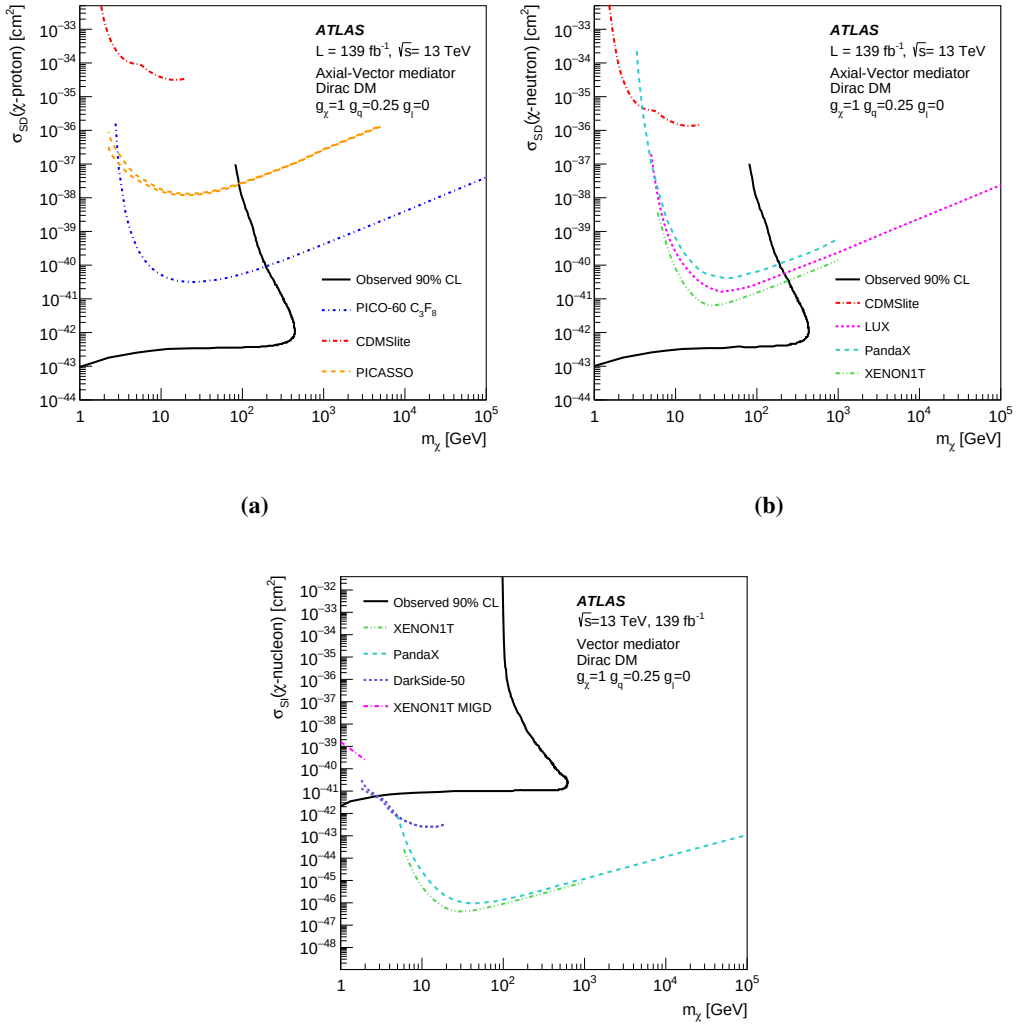

Figure 5: Comparison between this analysis and results from direct detection spin-dependent ([23–28]) and spin-independent ([29–32]) experiments. The 90% CL exclusion limits are shown, as a function of m_χ, on χ–proton (a) and χ–neutron (b) spin-dependent (SD) scattering cross section for axial-vector mediator, and on χ–nucleon spin-independent (SI) scattering cross section (c) for vector mediator. The considered couplings are g_q= 0.25, g_χ= 1 and g_l= 0 [3].

0.25, g_χ= 1 and g_l= 0. With the exception of m_χ lower than about 2 GeV, direct detection searches ([29–32]) provide stronger limits.

The upper limits on ALPs production are shown as a function of f_a and $c_{\tilde{W}}$ in fig. 6: the limit on $c_{\tilde{W}}$ is observed to increase linearly with f_a, with $c_{\tilde{W}} > 0.12$ excluded at 95% CL for $f_a = 1$ TeV. The two bands correspond to respectively $\pm1\sigma$ and $\pm2\sigma$ variations, and a 20% theoretical uncertainty on the signal, evaluated considering the same sources of uncertainties as for the simplified DM model, is included.

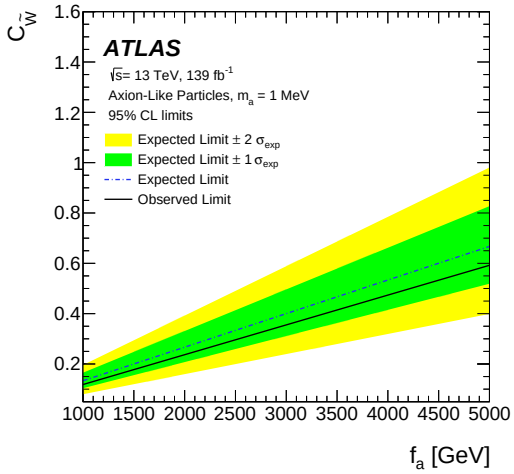

Figure 6: Observed (solid line) and expected (dot-dashed line) exclusions at 95% CL on the coupling $c_{\tilde{W}}$ as a function of the effective scale f_a for an ALP mass of 1 MeV. The region above the limit lines is excluded [3].

7.2 Model-independent limits

Model-independent limits on the visible cross section of new physics are provided, in order to allow reinterpretations in terms of signal models not considered in this analysis. A profile-likelihood-ratio test is performed, based on single-bin fits in each inclusive and exclusive $E_{\mathrm{T}}^{\mathrm{miss}}$ bin, including both SRs and CRs and enabling a signal component. The upper limits on the number of signal events can be rescaled to the integrated luminosity of the dataset, providing the upper limits on the visible cross section of new physics, $\sigma \times A \times \epsilon$, where σ is the production cross section, A the fiducial acceptance (*i.e.* the acceptance in a fiducial region defined at particle-level, applying same selection criteria as in SRs, but without accounting for detector effects) and ϵ the reconstruction or fiducial efficiency (which can be evaluated as the ratio between the particle-level and reconstruction-level acceptances). Table 3 reports the expected and observed limits on the visible cross section, as well as the observed ones on the number of events, for each $E_{\mathrm{T}}^{\mathrm{miss}}$ bin. The lowest reconstruction efficiency among all signals is also reported and can be used to straightforwardly derive an upper limit on the fiducial cross section, $\sigma \times A$.

8. Conclusions

A search for an excess of events in final states with one photon and missing transverse momentum ($E_{\mathrm{T}}^{\mathrm{miss}}$), with respect to Standard Model (SM) expectation, has been performed in proton-proton collisions at a centre-of-mass energy of 13 TeV, using 139 fb^{-1} of data collected by the ATLAS detector at the LHC.

Seven Signal Regions (SRs) are defined, with different $E_{\mathrm{T}}^{\mathrm{miss}}$ selection criteria. No excess is observed, and the results are interpreted in terms of exclusion limits.

The model-independent 95% CL upper limits on the visible cross section of Beyond Standard Model (BSM) events ranges from 2.45 to 0.53 fb, depending on the considered $E_{\mathrm{T}}^{\mathrm{miss}}$ bin. In

Table 3: Upper limits at 95% CL on the visible cross section $\sigma \times A \times \epsilon$ (observed and expected) and on the number of events (observed), and fiducial efficiencies, ϵ [3].

Signal region	$(\sigma \times A \times \epsilon)^{95}_{\text{obs}}$ [fb]	$(\sigma \times A \times \epsilon)^{95}_{\text{exp}}$ [fb]	N^{95}_{obs}	ϵ [%]
SRI1	2.45	$2.82^{+1.08}_{-0.78}$	340	76
SRI2	1.42	$1.68^{+0.63}_{-0.46}$	198	74
SRI3	0.93	$1.07^{+0.40}_{-0.29}$	129	72
SRI4	0.53	$0.63^{+0.23}_{-0.17}$	74	67
SRE1	1.80	$2.03^{+0.77}_{-0.56}$	250	75
SRE2	1.04	$1.15^{+0.43}_{-0.31}$	145	75
SRE3	0.79	$0.82^{+0.31}_{-0.22}$	109	71

addition, model-dependent 95% CL limits are set, in the m_χ-m_{med} plane, on the production of Weakly Interacting Massive Particles (WIMPs) in simplified Dark Matter (DM) models, predicting DM production via an s-channel exchange of a vector or axial-vector mediator. In the axial-vector (vector) scenario, DM candidates are excluded for masses up to 415 (580) GeV for axial-vector (vector) mediators, and mediator masses are excluded up to 1460 (1470) GeV. These results improve previous limits set using 36.2 fb^{-1} dataset. The results are also translated into limits on the $c_{\tilde{W}}$ parameter of an Axion Like Particle (ALP) production model, as a function of the effective scale f_a. Values of $c_{\tilde{W}} > 0.12$ are excluded at 95% CL for an ALP mass of 1 MeV and $f_a = 1$ TeV.

References

[1] K. Freese, *Status of Dark Matter in the Universe*, *Int. J. Mod. Phys.* **1** (2017) 325 [1701.01840].

[2] J. Goodman, M. Ibe, A. Rajaraman, W. Shepherd, T.M.P. Tait and H.-B. Yu, *Constraints on dark matter from colliders*, *Phys. Rev. D* **82** (2010) 116010 [1008.1783].

[3] ATLAS collaboration, *Search for dark matter in association with an energetic photon in pp collisions at $\sqrt{s} = 13$ TeV with the ATLAS detector*, *JHEP* **02** (2021) 226 [2011.05259].

[4] ATLAS Collaboration, *Search for dark matter at $\sqrt{s} = 13$ tev in final states containing an energetic photon and large missing transverse momentum with the atlas detector*, *Eur. Phys. J. C* **77** (2017) 393 [1704.03848].

[5] ATLAS collaboration, "Dark matter summary plots for s-channel mediators." ATL-PHYS-PUB-2021-006, Mar, 2021. http://cds.cern.ch/record/2758386.

[6] ATLAS collaboration, *The ATLAS experiment at the CERN large hadron collider*, *Journal of Instrumentation* **3** (2008) S08003.

[7] I. Brivio, M.B. Gavela, L. Merlo, K. Mimasu, J.M. No, R. del Rey et al., *ALPs effective field theory and collider signatures*, *Eur. Phys. J. C* **77** (2017) 572 [1701.05379].

[8] J. Abdallah et al., *Simplified models for dark matter searches at the LHC*, *Phys. Dark Univ.* **9-10** (2015) 8 [1506.03116].

[9] D. Abercrombie et al., *Dark Matter benchmark models for early LHC Run-2 Searches: Report of the ATLAS/CMS Dark Matter Forum*, *Phys. Dark Univ.* **27** (2020) 100371 [1507.00966].

[10] R.D. Peccei and H.R. Quinn, CP *conservation in the presence of pseudoparticles*, *Phys. Rev. Lett.* **38** (1977) 1440.

[11] M. Bauer, M. Heiles, M. Neubert and A. Thamm, *Axion-like particles at future colliders*, *Eur. Phys. J. C* **79** (2019) 74 [1808.10323].

[12] GEANT4 collaboration, *GEANT4: A Simulation toolkit*, *Nucl. Instrum. Methods Phys. Res., Sect. A* **506** (2003) 250.

[13] ATLAS collaboration, *The ATLAS Simulation Infrastructure*, *Eur. Phys. J. C* **70** (2010) 823 [1005.4568].

[14] J. Alwall, R. Frederix, S. Frixione, V. Hirschi, F. Maltoni, O. Mattelaer et al., *The automated computation of tree-level and next-to-leading order differential cross sections, and their matching to parton shower simulations*, *JHEP* **07** (2014) 079 [1405.0301].

[15] T. Sjöstrand, S. Mrenna and P. Skands, *A brief introduction to pythia 8.1*, *Comput. Phys. Comm.* **178** (2008) 852 [0710.3820].

[16] ATLAS Collaboration, *Performance of missing transverse momentum reconstruction wth the ATLAS detector using proton-proton collisions at* $\sqrt{s}$ = 13 *TeV*, *Eur. Phys. J. C* **78** (2018) 903 [1802.08168].

[17] ATLAS Collaboration, "Object-based missing transverse momentum significance in the ATLAS Detector." ATLAS-CONF-2018-038, 2018. https://cds.cern.ch/record/2630948.

[18] M. Baak et al., *Histfitter software framework for statistical data analysis*, *Eur. Phys. J. C* **75** (2015) 153 [1410.1280].

[19] A.L. Read, *Presentation of search results: the* cl_s *technique*, *J. Phys. G* **28** (2002) 2693.

[20] F. Kahlhoefer, K. Schmidt-Hoberg, T. Schwetz and S. Vogl, *Implications of unitarity and gauge invariance for simplified dark matter models*, *JHEP* **02** (2016) 016 [1510.02110].

[21] Planck collaboration, *Planck 2015 results. XIII. Cosmological parameters*, *Astron. Astrophys.* **594** (2016) A13 [1502.01589].

[22] A. Boveia et al., *Recommendations on presenting LHC searches for missing transverse energy signals using simplified s-channel models of dark matter*, *Phys. Dark Univ.* **27** (2020) 100365 [1603.04156].

[23] PICASSO Collaboration, *Final results of the picasso dark matter search experiment*, *Astropart. Phys.* **90** (2017) 85 [1611.01499].

[24] XENON Collaboration, *Constraining the spin-dependent wimp-nucleon cross sections with xenon1t*, *Phys. Rev. Lett.* **122** (2019) 141301 [1902.03234].

[25] SuperCDMS Collaboration, *Low-mass dark matter search with cdmslite*, *Phys. Rev. D* **97** (2018) 022002 [1707.01632].

[26] LUX Collaboration, *Limits on spin-dependent wimp-nucleon cross section obtained from the complete lux exposure*, *Phys. Rev. Lett.* **118** (2017) 251302 [1705.03380].

[27] PICO Collaboration, *Dark matter search results from the complete exposure of the pico-60 c_3f_8 bubble chamber*, *Phys. Rev. D* **100** (2019) 022001.

[28] PandaX-II Collaboration, *Spin-dependent weakly-interacting-massive-particle–nucleon cross section limits from first data of pandax-ii experiment*, *Phys. Rev. Lett.* **118** (2017) 071301 [1611.06553v3].

[29] XENON Collaboration, *Dark matter search results from a ton-year exposure of xenon1t*, *Phys. Rev. Lett.* **121** (2018) 111302 [1805.12562v2].

[30] XENON Collaboration, *Search for light dark matter interactions enhanced by the migdal effect or bremsstrahlung in xenon1t*, *Phys. Rev. Lett.* **123** (2019) 241803 [1907.12771].

[31] PandaX-II Collaboration, *Dark matter results from 54-ton-day exposure of pandax-ii experiment*, *Phys. Rev. Lett.* **119** (2017) 181302 [1708.06917v2].

[32] DarkSide Collaboration, *Low-mass dark matter search with the darkside-50 experiment*, *Phys. Rev. Lett.* **121** (2018) 081307 [1802.06994v3].

PoS(CORFU2021)098